ACS APPLIED MATERIALS & INTERFACES

Research Article

www.acsami.org

The Influence of Structure and Processing on the Behavior of TiO_2 Protective Layers for Stabilization of n-Si/TiO_2/Ni Photoanodes for Water Oxidation

Matthew T. McDowell,[†,‡] Michael F. Lichterman,[†,‡] Azhar I. Carim,[†] Rui Liu,[†,‡] Shu Hu,[†,‡] Bruce S. Brunschwig,[‡,§] and Nathan S. Lewis*[,†,‡,§,∥]

[†]Division of Chemistry and Chemical Engineering, California Institute of Technology, 210 Noyes Laboratory, Pasadena, California 91125, United States

[‡]Joint Center for Artificial Photosynthesis, California Institute of Technology, 1200 E. California Blvd., Pasadena, California 91125, United States

[§]Beckman Institute, California Institute of Technology, Pasadena, California 91125, United States

[∥]Kavli Nanoscience Institute, California Institute of Technology, Pasadena, California 91125, United States

Supporting Information

ABSTRACT: Light absorbers with moderate band gaps (1−2 eV) are required for high-efficiency solar fuels devices, but most semiconducting photoanodes undergo photocorrosion or passivation in aqueous solution. Amorphous TiO_2 deposited by atomic-layer deposition (ALD) onto various n-type semiconductors (Si, GaAs, GaP, and CdTe) and coated with thin films or islands of Ni produces efficient, stable photoanodes for water oxidation, with the TiO_2 films protecting the underlying semiconductor from photocorrosion in pH = 14 KOH(aq). The links between the electronic properties of the TiO_2 in these electrodes and the structure and energetic defect states of the material are not yet well-elucidated. We show herein that TiO_2 films with a variety of crystal structures and midgap defect state distributions, deposited using both ALD and sputtering, form rectifying junctions with n-Si and are highly conductive toward photogenerated carriers in n-Si/TiO_2/Ni photoanodes. Moreover, the photovoltage of these electrodes can be modified by annealing the TiO_2 in reducing or oxidizing environments. All of the polycrystalline TiO_2 films with compact grain boundaries investigated herein protected the n-Si photoanodes against photocorrosion in pH = 14 KOH(aq). Hence, in these devices, conduction through the TiO_2 layer is neither specific to a particular amorphous or crystalline structure nor determined wholly by a particular extrinsic dopant impurity. The coupled structural and energetic properties of TiO_2, and potentially other protective oxides, can therefore be controlled to yield optimized photoelectrode performance.

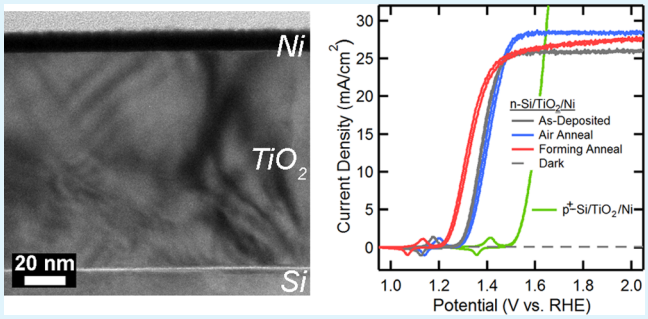

KEYWORDS: *water splitting, photoelectrochemistry, photocorrosion, solar fuels, heterojunction interfaces, oxygen evolution reaction*

INTRODUCTION

Efficient conversion of solar energy into hydrogen or hydrocarbons via the electrochemical reduction of protons and/or carbon dioxide is a promising, carbon-neutral route to the production of storable transportation fuels.[1,2] An attractive system for the generation of solar fuels is an integrated light-absorbing/fuel-forming photoelectrochemical (PEC) device based on dual semiconducting light absorbers.[3,4] In any fuel-producing (photo)electrochemical system, the oxidation of water to oxygen gas at the anode is required to liberate the electrons needed for the reduction of water and/or carbon dioxide at the cathode. The potentials necessary for the oxidation of water, in conjunction with the acidic or alkaline electrolytes that are often required for efficient and intrinsically safe system operation, lead to (photo)corrosion of the majority of semiconductors as well as the corrosion of many catalysts used for the generation of solar fuels. Most technologically relevant semiconductors (including Si, GaAs, and CdTe) are unstable in aqueous alkaline solutions, through either dissolution or passivation. Although some oxide semiconductors (such as TiO_2 and $SrTiO_3$) are stable under anodic potentials in alkaline conditions,[5,6] the band gaps of these oxide semiconductors (E_g = 3−3.5 eV) are too high for the materials to absorb enough of the solar spectrum for efficient sunlight-driven production of fuels. Thus, strategies for stabilizing

Received: January 13, 2015
Accepted: June 17, 2015
Published: June 17, 2015

DOI: 10.1021/acsami.5b00379
ACS Appl. Mater. Interfaces 2015, 7, 15189−15199

materials with moderate band gaps (E_g = 1−2 eV) are critical for the development of solar fuels devices.

Various semiconductors have recently been combined with protective materials to form stable photoanodes for water oxidation.[7−17] These systems generally consist of an n-type semiconductor with a moderate band gap as the primary light absorber, combined with a ∼1−200 nm thick metal oxide or metal overlayer that protects the underlying semiconductor from photocorrosion and catalyzes the oxidation of water. The protective layer needs to (i) be conductive for anodic current; (ii) allow for appropriate band bending at the solid-state and solid/liquid junctions to obtain efficient photogenerated carrier transport from the semiconductor to the solution; (iii) transmit a significant portion of the visible spectrum; and (iv) be chemically stable toward corrosion in an aqueous environment. Ultrathin (a few nm) oxides and metals have been shown to fulfill some of these requirements,[7,10,18] but in many cases the stability imparted by an ultrathin film is limited due to naturally occurring pinholes and defects. In contrast, amorphous TiO_2 films up to 150 nm in thickness deposited on n-Si by atomic-layer deposition (ALD), and coated with a ∼3−5 nm Ni catalytic overlayer, have recently been shown to exhibit good performance as photoanodes for photodriven water oxidation, yielding >100 h of photocurrent stability in 1.0 M KOH electrolyte.[12] TiO_2 is thermodynamically stable in alkaline environments at positive potentials, and it protects the underlying Si by preventing contact with the electrolyte. Other n-type semiconductors (GaP, CdTe) coated with amorphous TiO_2 films have also been shown to exhibit similar, stable electrochemical performance.[12,13] Based on the large band gap of TiO_2 (E_g = 3.3 eV) compared to Si (E_g = 1.1 eV), in conjunction with the significant (2.2 eV) offset between the valence bands (VB) of Si and TiO_2,[12] an ideal n-Si/TiO_2/Ni structure would not be expected to conduct photogenerated holes from the Si through the TiO_2 to the catalyst/electrolyte interface. A possible mechanism for conduction of photogenerated carriers through the TiO_2 layer is for hole transport to be facilitated by midgap defect states in the TiO_2;[12] a recent density functional theory (DFT) study has shown such a mechanism to be plausible.[19] These defect states could arise due to the amorphous structure and/or the presence of carbon or nitrogen impurities from the ALD process.[12] A similar conduction mechanism has been proposed in other related research on water-oxidation photoanodes.[8] In addition, studies of TiO_2 as a gate dielectric have shown that TiO_2 can be "leaky" with respect to electronic conduction, which has often been attributed to high concentrations of Ti^{3+} or other electronic defects.[20−24]

TiO_2 is a versatile material that features a stable amorphous structure as well as various crystalline phases, of which anatase and rutile are the most common. As in many metal oxides, the concentration of oxygen vacancies (which can vary depending on fabrication methods and processing conditions) controls the concentration of free carriers and thus the conductivity. Furthermore, Ti^{3+} arising from oxygen vacancies or a disordered structure can create energetic defect states within the band gap.[8,25,26] The recent results showing that amorphous TiO_2 protection layers modified by Ni films or islands can conduct anodic currents[12] prompt questions regarding the relationship between the crystal structure, electronic characteristics, and fabrication method of TiO_2 films used as protective conductive layers on n-Si photoelectrodes. A particular point of interest is the relationship between the crystal structure and materials properties of TiO_2 that affect the photogenerated carrier conduction and junction characteristics in these devices. Also of interest is whether amorphous films are unique in their performance or whether crystalline TiO_2 films exhibit similar nonideal hole-transport behavior. We demonstrate herein that both crystalline and amorphous TiO_2 films with varying electronic properties form effective heterojunction partners with n-Si photoanodes. Furthermore, we demonstrate that the energetic properties of the n-Si/TiO_2 interface can be tuned via annealing in different chemical environments, and that TiO_2 layers with different crystal structures and grain-boundary morphologies are all highly protective against photocorrosion in 1.0 M KOH(aq), except when the fabrication method yields films that have significant void space between the grains in the protective layer. These results indicate that carrier conduction in n-Si/TiO_2/Ni devices is not limited to amorphous TiO_2 deposited by ALD, and that the properties of TiO_2, and perhaps other oxides, can be tuned so that such films behave as effective protective heterojunction partners with n-Si as photoanodes for water oxidation.

METHODS

TiO_2 films were deposited on n-Si(111) wafers (resistivity = 0.5 Ω·cm) or p^+-Si(111) wafers (resistivity = 0.005 Ω·cm) by either ALD or DC magnetron sputtering. Immediately before deposition, the wafers were cleaned using an RCA etch process that consisted of (i) soaking in a 5:1:1 $H_2O/H_2O_2/NH_4OH$ solution at 75 °C for 10 min; (ii) etching the native oxide from the wafers with 10 vol % HF; and then (iii) soaking in a 5:1:1 H_2O/H_2O_2/HCl solution at 75 °C for 10 min. The last step removes ionic contaminants and results in controlled growth of a passivating SiO_x film. This step is important for reproducibility, because SiO_x layers will be produced during ALD or sputter deposition of TiO_2 on etched or H-terminated Si surfaces. Films were deposited by ALD using either tetrakis-dimethylamidotitanium (TDMAT, Sigma-Aldrich, 99.999%) or titanium tetraisopropoxide (TTIP, Strem Chemicals, 98%) as precursors. Water (18.2 MΩ·cm resistivity, Millipore) was used as the other reactant for ALD growth. For the TDMAT-ALD process, the Si wafers were held at 150 °C, while for the TTIP-ALD process, the wafers were held at 250 °C. Sputtered samples were fabricated using a Ti metal target (ACI Alloys, 99.95%) in a mixed O_2−Ar plasma using a DC power source, with the sample held at 400 °C in the sputtering chamber during deposition. Some samples that were deposited via ALD using the TDMAT precursor were subjected to postdeposition anneals in either forming gas (5% H_2, 95% N_2) or air for 1 h at temperatures between 400 and 775 °C. Full experimental details are presented in the Supporting Information.

Electrodes were fabricated by first cleaving the Si/TiO_2 samples into pieces, and then sputtering a ∼5−8 nm layer of Ni metal onto the Si/TiO_2 samples using a Ni target and RF magnetron sputtering. The edges of each wafer piece were masked with polyimide tape (Kapton) to avoid Ni deposition onto the bare Si. The back side of each sample was then scribed with an In−Ga eutectic alloy (Alfa-Aesar, 99.99%) to make ohmic contact, and then the In−Ga-contacted electrode was affixed to a Sn-coated Cu wire with conductive Ag paint (SPI, Inc.). The Cu wire was threaded through a glass tube, and after the Ag paint was dry, the electrode was sealed to the glass using epoxy (Loctite Hysol 9460). The back and edges of the Si, along with the exposed wire, were all covered with epoxy so that only a portion of the front of the electrode was exposed. The exposed active area of each electrode was measured with an optical scanner (Epson Perfection V370 in conjunction with ImageJ software), and the electrode areas were between 0.05 and 0.1 cm^2.

Photoelectrochemistry was either performed in pH = 14 electrolyte (1.0 M KOH, Macron Chemicals, >88%) or in an aqueous $Fe(CN)_6^{3-/4-}$ electrolyte that consisted of 0.35 M $K_4Fe(CN)_6$ (Acros Organics, >99%) and 0.050 M $K_3Fe(CN)_6$ (Fisher Scientific,

DOI: 10.1021/acsami.5b00379
ACS Appl. Mater. Interfaces 2015, 7, 15189−15199

99.4%). The experiments in KOH(aq) were performed using a three-necked, round-bottom, 50 mL flask equipped with a planar quartz window for illumination. A Pt gauze (Aldrich) counter electrode was separated from the main compartment by a glass frit, and a Hg/HgO (1.0 M KOH) or a saturated calomel electrode (SCE) (CH Instruments) was used as the reference electrode. Electrode potentials in 1.0 M KOH(aq) were converted to the reversible hydrogen electrode (RHE) scale using $E_{RHE} = E_{SCE} + 0.244 + 0.0591 \cdot pH$, or $E_{RHE} = E_{Hg/HgO} + 0.098 + 0.0591 \cdot pH$ at $T = 25$ °C, and the potentials herein are reported vs RHE. The $Fe(CN)_6^{3-/4-}$ experiments were performed in a three-necked flat-bottom flask with a planar glass window on the side for illumination. A Pt gauze was the counter electrode and a 1.0 M Ag/AgCl was the reference electrode (CH Instruments). A 150 W Xe lamp (Newport 6255) coupled with an AM1.5 global filter (Newport 81094) and quartz diffuser were utilized for illumination of the working electrode, but the diffuser was removed for evaluation of the photoelectrode performance in the $Fe(CN)_6^{3-/4-}$ electrolyte. For calibration of the light intensity at the location of the photoelectrode, a Si photodiode was placed within the electrolyte in the cell before testing, and the photodiode indicated that the light intensity was ~100 mW cm^{-2}. Cyclic voltammetry was performed by sweeping the potential of the working electrode at a rate of 40 mV s^{-1} using a Bio-Logic SP-200 potentiostat.

The samples were further characterized with X-ray diffraction (XRD), Raman spectroscopy, X-ray photoelectron spectroscopy (XPS), cross-sectional transmission electron microscopy (TEM), impedance spectroscopy, and secondary ion mass spectrometry (SIMS). Details regarding these experiments are presented in the Supporting Information.

RESULTS

As-deposited amorphous TiO_2 coatings, prepared using the same TDMAT precursor and growth process as described previously,[12] were annealed in either air or forming gas. The Raman spectra of the as-deposited unannealed films (Figure 1a) did not show any Raman modes of a crystalline TiO_2 phase, suggesting that the films were amorphous. The Raman spectra of the annealed films (Figure 1a) exhibited the characteristic modes of the anatase phase of TiO_2.[27] XRD data (see Supporting Information Figures S1 and S2) also indicated that samples annealed between 400 and 500 °C in air or in forming gas converted to the crystalline anatase phase. The as-deposited and annealed films exhibited mutually similar Ti 2p XPS signals (Figure 1b), with Ti $2p_{3/2}$ peaks at 458.9–459.0 eV arising from Ti^{4+} species. Ti^{3+} shoulders were not detectable in the spectra, indicating that any annealing-induced changes in the concentration of oxygen vacancies were below the XPS detection limit. The detection limit is related to the relative area of the peaks arising from different oxidation states; thus, to detect a minority oxidation state, it must be present with a concentration of ~1%.

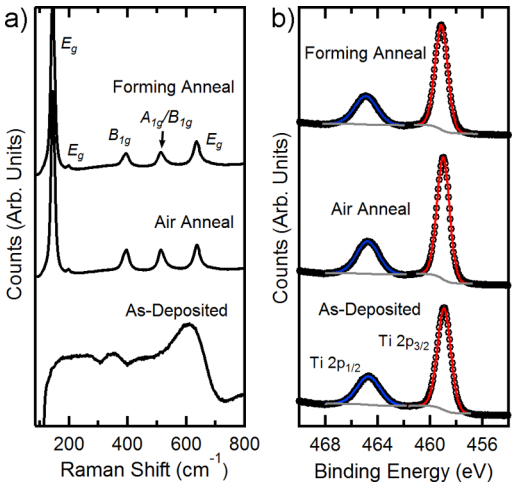

Figure 1. (a) Raman spectra of TiO_2 films deposited via ALD with the TDMAT precursor and annealed in different environments. The bottom trace is from as-deposited TiO_2, and does not display Raman modes arising from any TiO_2 crystalline phase. The samples annealed at 500 °C in air or in forming gas (top two traces) both showed similar peaks, which correspond to the Raman modes of the anatase phase of TiO_2. (b) Ti 2p XPS spectra of each of the TDMAT-ALD films. The peak positions correspond to Ti^{4+}, with no observable Ti^{3+} shoulder present.

Figure 2a compares the photoelectrochemical behavior of the annealed and as-deposited TiO_2 films when used as a component of n-Si/TiO_2/Ni photoanodes. The TiO_2 layer was grown to be ~105 nm in thickness by use of 2350 ALD cycles. In 1.0 M KOH(aq) under simulated 1-sun illumination, the crystalline samples (annealed at 450 °C) exhibited comparable current density vs potential (J–E) characteristics to those observed from the as-deposited amorphous TiO_2 films. The fill factors and light-limited current densities of these three types of samples were mutually similar, indicating that the crystalline and amorphous TiO_2 samples had similar carrier-conduction properties in these devices. However, a noticeable slope was observed in the light-limited current region of the forming-gas annealed sample due to an increase in dark current that was present in many of the electrodes that had been annealed in forming gas. The light-limited currents produced by photoanodes coated with the as-deposited amorphous samples (~26 mA cm^{-2} at 1 sun) were within 10% of previously measured values from similar devices, when corrected for the difference in light intensity between the two different test conditions (the previous measurements were performed at 1.25 suns).[12]

Figure 2a indicates that the forming-gas annealed n-Si/TiO_2 sample exhibited a larger photovoltage than the as-deposited or air-annealed n-Si/TiO_2 samples, when compared to the dark behavior of a p^+-Si/TiO_2/Ni electrode. Such a trend in photovoltage was confirmed by evaluating the electrochemical behavior of the n-Si/TiO_2/Ni photoanodes in contact with the kinetically reversible, one-electron $Fe(CN)_6^{3-/4-}$(aq) redox couple (Figure 2b, c). The three different samples showed mutually similar fill factors, but the forming-gas annealed sample exhibited a higher open-circuit voltage (V_{oc}) than the other two samples (Figure 2b). Figure 2c presents a plot of the V_{oc} values under illumination for a number of samples (as-deposited and annealed at various temperatures between 400 and 500 °C), clearly indicating an increase in V_{oc} of the forming-gas annealed samples relative to the as-deposited or air-annealed samples. Variations in the cleaning and in the TDMAT-ALD growth process can cause variations in V_{oc} of as-deposited TDMAT-ALD electrodes. To control for this possible variability, all of the samples in Figure 2 were produced in the same ALD growth run. The V_{oc} values in Figure 2c are slightly lower than those reported previously,[12] but the comparison between samples in a common growth run allows for focusing on the trends in photovoltage as the annealing conditions were varied as specified.

Although these data indicate that both amorphous and annealed TiO_2 films yielded similar photoanodic electrochemical behavior in conjunction with n-Si, the electrochemical and structural data do not preclude a situation in which

DOI: 10.1021/acsami.5b00379
ACS Appl. Mater. Interfaces 2015, 7, 15189–15199

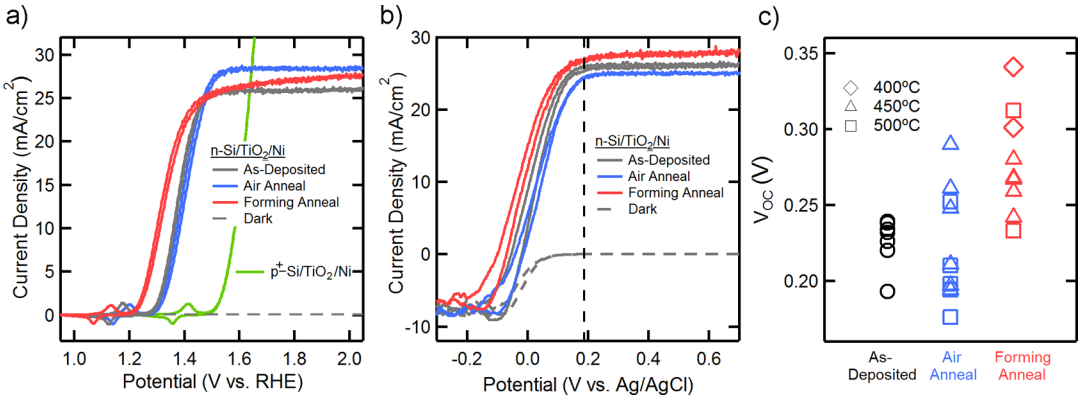

Figure 2. Photoelectrochemical behavior of n-Si/TiO_2/Ni electrodes fabricated using ALD of TiO_2 (TDMAT precursor) followed by annealing at $T \leq 500$ °C under different conditions. The as-deposited thickness of the TiO_2 was 105 nm. (a) $J-E$ data for n-Si/TiO_2/Ni electrodes under 1-sun illumination in 1.0 M KOH(aq). The annealed samples were heated at 450 °C. The $J-E$ data of the n-Si/TiO_2/Ni samples were from the 25th cycle, after the transformation of the surface layer of Ni to form catalytically active Ni(Fe)OOH for water oxidation (the Fe is incorporated from impurities in the electrolyte).[28,29] The dark behavior is from the as-deposited sample. A p^+-Si/TiO_2/Ni sample with as-deposited TiO_2 (green) is shown as a dark catalytic electrode for reference. Note that the anodic and cathodic redox features visible at potentials negative of the water oxidation potential are due to transformation between Ni^{2+} and Ni^{3+} in the catalytic layer.[29] (b) Typical $J-E$ data of n-Si/TiO_2/Ni electrodes under 1-sun illumination in aqueous 0.35 M $K_4Fe(CN)_6$/0.050 M $K_3Fe(CN)_6$(aq). The vertical dashed line denotes the Nernstian potential of the $Fe(CN)_6^{3-/4-}$ electrolyte. (c) Measured open-circuit voltage (V_{oc}) values of n-Si/TiO_2/Ni samples annealed under various conditions and tested in 0.35 M $K_4Fe(CN)_6$/0.050 M $K_3Fe(CN)_6$(aq) under illumination.

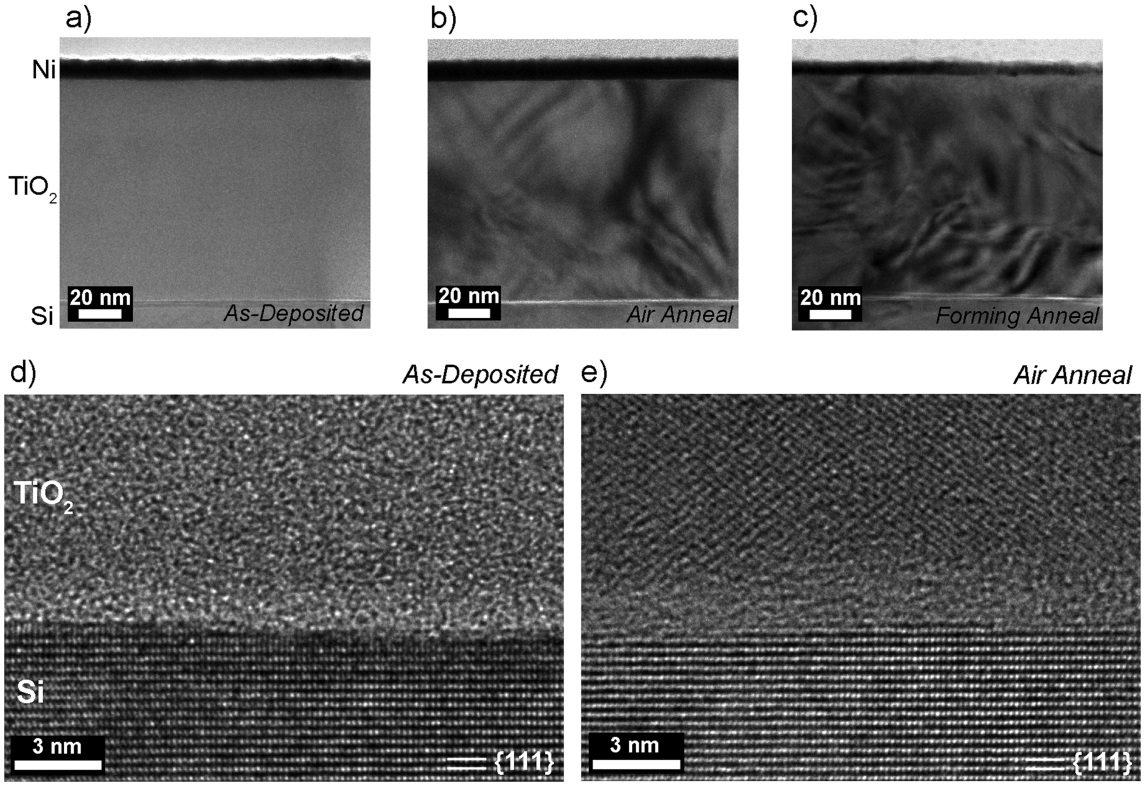

Figure 3. Cross-sectional TEM characterization of TDMAT-ALD TiO_2 films (2350 ALD cycles) on Si. (a–c) Low-magnification images of the cross sections of (a) as-deposited TiO_2, (b) TiO_2 annealed in air at 500 °C, and (c) TiO_2 annealed in forming gas at 500 °C. The dark layer at the top of the images is the sputtered Ni layer. (d) High-resolution image of the Si/TiO_2 interface in the as-deposited film. The TiO_2 film is amorphous. (e) High-resolution image of the Si/TiO_2 interface in the air-annealed film. Lattice fringes in the TiO_2 are visible, as well as an amorphous SiO_x interfacial layer.

annealing generates a mixed crystalline/amorphous phase that exhibits preferential conduction due to the amorphous regions. To investigate this possibility, and to examine the nanoscale structure and morphology of the electrodes, cross-sectional TEM was performed on Si/TiO_2/Ni samples that included either as-deposited or annealed TiO_2. Figure 3a–c shows low-magnification cross-sectional images of as-deposited (a), air-annealed (b), and forming-gas annealed (c) TiO_2 samples (the annealing temperature was 500 °C). The as-deposited TiO_2 showed a featureless contrast indicative of an amorphous material, whereas the annealed samples exhibited a characteristic "wavy" contrast that is indicative of slight strain or bending

DOI: 10.1021/acsami.5b00379
ACS Appl. Mater. Interfaces 2015, 7, 15189–15199

in a crystal. The annealed TiO_2 was comprised of anatase crystals that spanned the ~100 nm thickness of the film and that were microns wide (see Supporting Information Figure S3 for a low-magnification image showing the polycrystalline nature of the films). No disordered regions were detected in the annealed TiO_2, indicating that carrier conduction must be occurring through the anatase crystals in these films. High-resolution (HR) TEM was also used to image the Si/TiO_2 interface in amorphous and annealed samples (Figure 3d and e). A lack of crystalline order was clearly evident in the as-deposited TiO_2 (Figure 3d), whereas lattice fringes in the TiO_2 were visible in the air-annealed sample (Figure 3e). In addition, an amorphous ~1.5−2 nm thick SiO_x interfacial layer was evident in the annealed sample (the average thickness of the interfacial layer calculated from different images was 1.9 ± 0.18 nm). A SiO_x layer was also present on the as-deposited sample (as seen by lighter contrast at the interface), but the thickness of the interfacial layer was more difficult to quantify in the as-deposited sample because the SiO_x-TiO_2 interface was not distinct, since both materials are amorphous. Image delocalization (an imaging artifact) may also contribute to the contrast at this interface.

To further explore the effect of structure and morphology on performance, TiO_2 films were fabricated using different methods to allow for comparison to the films that were deposited with TDMAT-ALD. TiO_2 films were grown using ALD with a different precursor (TTIP) and by sputtering, and these films were not annealed. As shown by the J−E data of n-Si/TiO_2/Ni electrodes in contact with $Fe(CN)_6^{3-/4-}$(aq) (Figure 4a), both the TTIP-ALD and sputtered TiO_2 films facilitated the formation of rectifying junctions. The fill factor and V_{oc} values of TTIP-ALD electrodes were similar to the values obtained from films produced by TDMAT-ALD (Figure 2). Sputtered TiO_2 samples consistently exhibited lower V_{oc} values than the ALD-produced films (the average V_{oc} of 16 samples with various TiO_2 thicknesses was 134 ± 20 mV). The sputtered films also had higher dark currents (usually a few mA cm^{-2}) and sloping light-limited photocurrents, presumably due to shunting. Similar behavior was observed when the electrodes were used for water oxidation in 1.0 M KOH (Figure 4b).

For the sputtered samples, the slope of the J−E data before the light-limited current density was reached was dependent on the thickness of the TiO_2 film (within the thickness range tested). This behavior is in contrast to the behavior of n-Si/TiO_2/Ni photoelectrodes prepared using TDMAT-ALD, which have previously been shown to exhibit slopes of their J−E curves that are independent of TiO_2 film thickness for thicknesses between ~4 and ~150 nm.[12] The sputtered films appeared to be more resistive as the film thickness increased from ~25 to ~185 nm (Supporting Information Figure S4); this result is confirmed by impedance spectroscopy of the different types of films shown in Supporting Information Figure S5. However, four-point probe measurements of these films revealed that the sputtered films were the most conductive, with a measured resistivity value of 4.28 Ω·cm. For comparison, the resistivity of the as-deposited TDMAT-ALD material was 215 Ω·cm. This behavior suggests that the four-point probe conductivity of the sputtered TiO_2 film does not correlate with the through-thickness conductance.

Figure 5 shows TEM and Raman spectroscopy of the sputtered and TTIP-ALD TiO_2 films, for comparison to the TiO_2 formed by TDMAT-ALD. The Raman spectrum of the TTIP-ALD film indicated that the TiO_2 layer was anatase, while

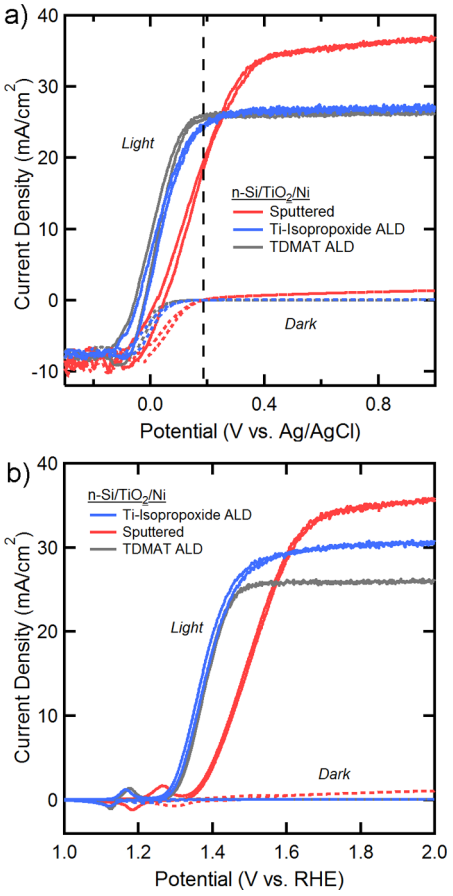

Figure 4. Photoelectrochemical characterization of n-Si/TiO_2/Ni electrodes with TiO_2 deposited via sputtering and by using ALD with a different precursor (TTIP). (a) Light and dark behavior of samples in 0.35 M $K_4Fe(CN)_6$/0.050 M $K_3Fe(CN)_6$(aq) electrolyte. A curve from an illuminated TDMAT-ALD electrode is included in the plot for comparison. (b) Light and dark behavior of samples in 1.0 M KOH(aq). The TTIP-ALD TiO_2 film had a thickness that varied from ~50 to ~150 nm, the sputtered sample was ~75 nm thick, and the TDMAT-ALD sample was ~100 nm thick.

the spectrum from the sputtered film revealed a mixture of anatase and rutile (Figure 5a). TEM imaging showed that the sputtered film was of uniform thickness and was made up of a multitude of columnar grains about 10−30 nm in width (Figure 5b); such a morphology is common for sputtered material.[30] The selected-area electron diffraction (SAED) pattern of a sputtered film (Figure 5e) showed a typical polycrystalline ring pattern with diffraction spots arising from both anatase and rutile, indicating that the crystallites were intimately mixed. HR imaging of the Si/TiO_2 interface in the sputtered film (Figure 5d) showed a SiO_x layer that was ~1.2−1.5 nm thick. The TTIP-ALD films were composed of anatase crystals that generally spanned the thickness of the film and were hundreds of nanometers to a few micrometers wide (Figure 5c and f). However, the thickness of the TTIP-ALD films was nonuniform (it ranged between 50 and 150 nm). These thickness variations suggest that under the conditions utilized, TTIP-ALD is not a true ALD growth process.[31] Pinholes and regions of void space were located between crystals, as shown by the vertical fissure in Figure 5c. XPS data on sputtered and TTIP-ALD TiO_2 samples showed that the Ti 2p peaks arose primarily from Ti^{4+} species, with no obvious Ti^{3+} shoulders (Supporting

DOI: 10.1021/acsami.5b00379
ACS Appl. Mater. Interfaces 2015, 7, 15189−15199

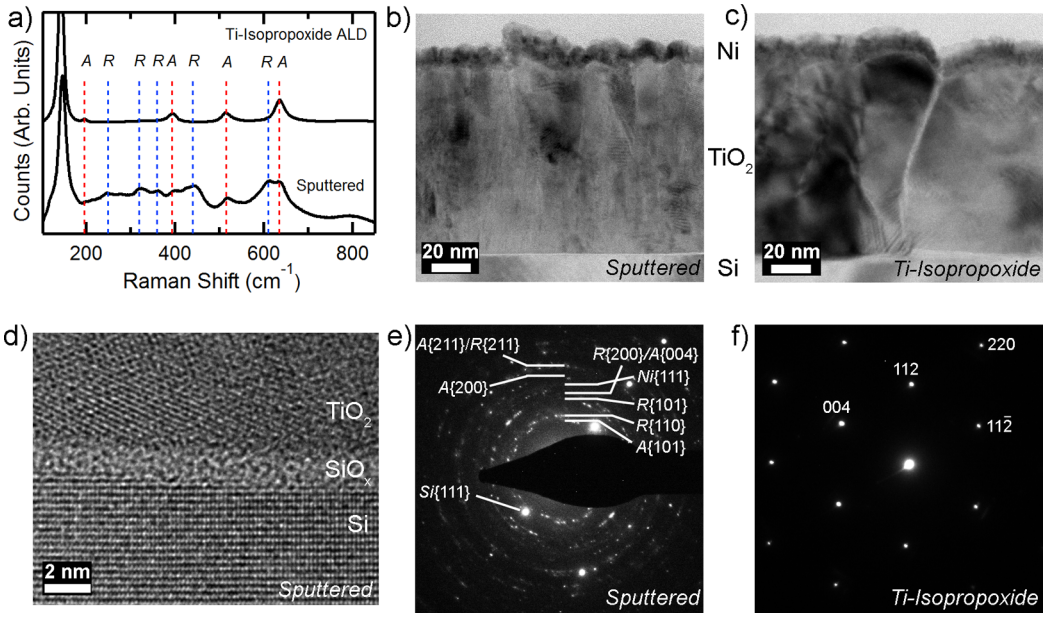

Figure 5. Structure of sputtered and TTIP-ALD TiO_2 films. (a) Raman spectroscopy showing that the TTIP-ALD film is anatase (top), while the sputtered film is a mixture of anatase and rutile. (b) Cross-sectional TEM image of a sputtered film showing columnar grains 10−30 nm in width. (c) Cross-sectional TEM image of a TTIP-ALD film showing larger crystals and a crack between crystals. (d) High-resolution TEM image of the Si/TiO_2 interface in a sputtered sample. (e) A selected-area electron diffraction (SAED) pattern of a sputtered film revealing diffraction rings corresponding to anatase (*A*), rutile (*R*), Ni (from the top surface of the TiO_2), and Si. (f) An SAED pattern of a TTIP-ALD film revealing diffraction spots from a single anatase crystal.

Information Figure S6), similar to the XPS data for the TDMAT-ALD samples.

To investigate the presence of defect states within the TiO_2 band gap, XPS valence-band spectra were collected from each of the TiO_2 films studied herein (Figure 6). In this type of experiment, the photoemission signal detected between the Fermi level (binding energy (BE) = 0 eV) and the valence-band onset (BE = ∼3.0−3.4 eV) corresponds to that from

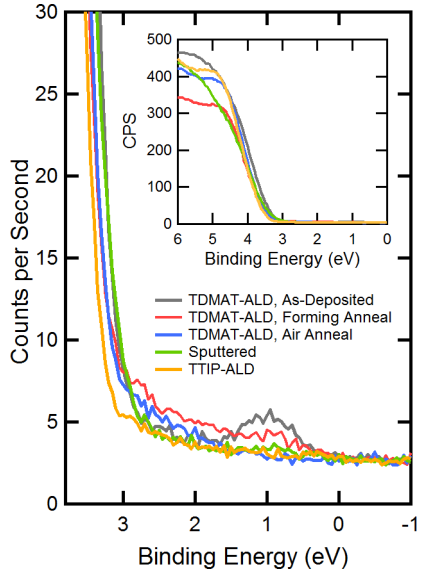

Figure 6. X-ray photoemission valence-band spectra of various TiO_2 materials. These spectra were collected from p^+-Si/TiO_2 samples. The main plot is a magnified view of the band gap region, and the inset is a full view of the valence-band onset. The annealed samples were heated at 450 °C for 1 h.

midgap defect states. The main plot in Figure 6 shows a magnified view of the band gap region, and the inset shows the full valence-band spectra. The amorphous, as-deposited TDMAT-ALD film showed a distinct signal centered around BE = 1 eV that corresponds to defect states near this energy position. This spectrum is similar to that previously reported for TDMAT-ALD TiO_2.[12] The forming-gas annealed TDMAT-ALD sample showed increased photoemission across a broader band of BE values, and the air-annealed TDMAT-ALD sample showed slightly increased photoemission near the valence-band onset. The sputtered and TTIP-ALD material both showed less substantial photoemission across the range of BE values within the band gap than materials prepared using TDMAT-ALD. These data indicate that the various TiO_2 materials studied herein had midgap defect states with different energy distributions and densities.

An important feature of the Si/TiO_2/Ni device structure for solar fuels applications is the protection against photocorrosion afforded by the combination of the underlying photoactive semiconductor with the wide band gap, corrosion-resistant TiO_2 and Ni-based water-oxidation catalyst. To probe stability during water oxidation, electrodes with each of the previously discussed types of TiO_2 were tested by holding the sample at a constant potential (1.85 V vs RHE) under simulated 1-sun illumination in a three-electrode configuration in 1.0 M KOH(aq) electrolyte. Previous work has shown that, under similar conditions, amorphous, conformal, TDMAT-ALD TiO_2 films provide >100 h stability on n-Si.[12] Figure 7 shows similar results for an n-Si/TiO_2/Ni electrode with amorphous ALD-deposited TiO_2, demonstrating that the sample retained 92% of its initial photocurrent after 60 h of continuous operation (the projected photocurrent at 100 h is quite similar to that reported previously[12]). Electrodes with annealed TDMAT-ALD TiO_2 as well as sputtered TiO_2 films also showed excellent stability (85−90% photocurrent retention after 60 h, Figure 7). In

DOI: 10.1021/acsami.5b00379
ACS Appl. Mater. Interfaces 2015, 7, 15189−15199

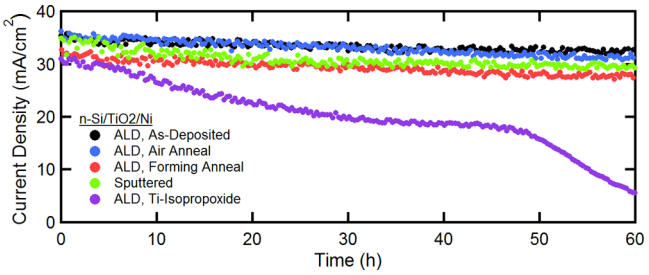

Figure 7. Potentiostatic stability tests of various n-Si/TiO_2/Ni samples during water oxidation in 1.0 M KOH(aq) under simulated 1-sun illumination. The electrodes were held at 1.85 V vs RHE. All films were ~100 nm thick except for the TTIP-ALD sample, for which the thickness varied within the sample from ~50 to ~150 nm.

contrast, all of the TTIP-ALD TiO_2 devices tested showed a steady decay in photocurrent. Optical microscopy of the TTIP-ALD devices after stability testing revealed significant damage to the TiO_2 films, with missing portions widely visible (see Supporting Information Figure S7 for comparative before-and-after images). The faradaic efficiency for O_2 production was not measured herein because it has been well established that stable Si/TiO_2/Ni electrodes (as well as TiO_2/Ni overlayers in conjunction with other underlying semiconductors) produce O_2 with approximately 100% faradaic efficiency under the conditions used herein.[12,13,32]

For comparison to these TiO_2 films that were deposited and processed at temperatures ≤500 °C, further experiments were carried out on TDMAT-ALD films annealed at higher temperatures. Annealing TiO_2 films at 600 °C in air and forming gas for 1 h resulted in the formation of anatase, with a minor rutile phase component in air-annealed films (Raman spectra of these films are presented in Supporting Information Figure S8). Annealing at 775 °C in air and forming gas for 1 h resulted in the formation of rutile with a minor anatase component. Figure 8 shows cyclic voltammograms of illuminated n-Si/TiO_2/Ni electrodes (Figure 8a) and dark p^+-Si/TiO_2/Ni electrodes (Figure 8b) that contain ~100 nm TiO_2 films that were annealed at 600 and 775 °C in air and forming gas.

Annealing at 600 °C in both air and forming gas resulted in an increase in resistance, with a more significant increase in resistance observed for the air-annealed samples. Further loss in conductivity was observed after higher-temperature anneals, with annealing at 775 °C in forming gas resulting in current densities of ~1 mA cm^{-2} at 0.8 V vs Ag/AgCl, whereas annealing at 775 °C in air resulted in current densities <1 μA cm^{-2} at 0.8 V vs Ag/AgCl. The poor conductivity of these electrodes contrasts with the facile conduction through films processed and annealed at temperatures ≤500 °C (Figures 2 and 4). Nyquist plots of the impedance spectra of the samples annealed at 600 and 775 °C showed two semicircles (Supporting Information Figure S5), indicating a series combination of two RC-components. This behavior is consistent with the growth of resistive SiO_x films at the Si/TiO_2 interface. The thicknesses of the SiO_x films were measured with cross-sectional HRTEM, and images of samples annealed under these four high-temperature conditions are presented in Supporting Information Figure S9. The images clearly show the growth of thick SiO_x interfacial films at 775 °C (both in air and forming gas), while the interfacial films of samples annealed at 600 °C had thicknesses $t \leq 2$ nm, only slightly thicker than the samples annealed at 500 °C. Average SiO_x thicknesses are tabulated in Table 1.

Table 1. Average SiO_x Interfacial Film Thicknesses on Si/TiO_2 Samples Annealed at Various Temperatures in Air and Forming Gas

	500 °C	600 °C	775 °C
air	1.9 ± 0.18 nm	2.0 ± 0.16 nm	6.0 ± 0.36 nm
forming gas	1.4 ± 0.15 nm	1.7 ± 0.16 nm	2.9 ± 0.39 nm

The relative amount of elemental impurities (carbon and nitrogen) within the various TiO_2 films was also evaluated to ascertain whether the impurity content correlates with the high conductivity of TDMAT-ALD films.[12] SIMS depth-profiling was performed on TDMAT-ALD films that were as-deposited and annealed at moderate and high temperatures, as well as on sputtered and TTIP-ALD films (Supporting Information Figures S11–S13). The TDMAT-ALD films contained very similar amounts of carbon for all annealing conditions, while the nitrogen content changed slightly with different annealing temperatures. The TTIP-ALD films contained less carbon and nitrogen than the TDMAT-ALD films, whereas the sputtered films contained higher concentrations of these impurities.

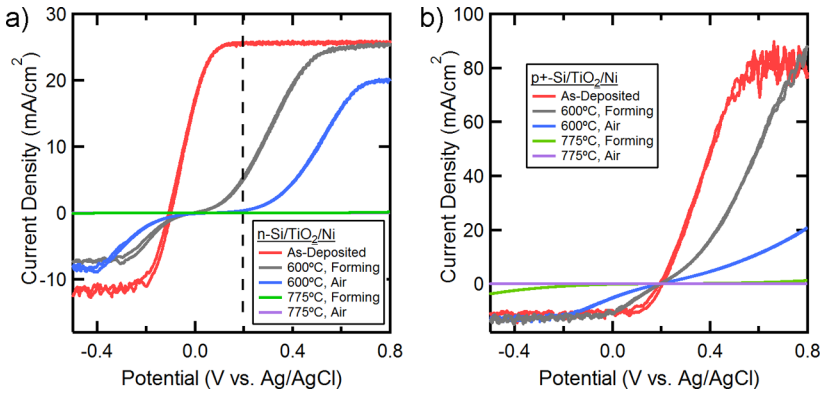

Figure 8. Cyclic voltammograms of Si/TiO_2/Ni electrodes with TDMAT-ALD TiO_2 annealed at higher temperatures in air and forming gas; the electrochemistry was performed in 0.35 M $K_4Fe(CN)_6$/0.050 M $K_3Fe(CN)_6$(aq) electrolyte. (a) n-Si/TiO_2/Ni electrodes under 1-sun illumination. (b) p^+-Si/TiO_2/Ni electrodes in the dark. The resistance increases with annealing temperature, with greater resistance in air-annealed samples.

DOI: 10.1021/acsami.5b00379
ACS Appl. Mater. Interfaces 2015, 7, 15189–15199

DISCUSSION

As shown herein, the annealing of amorphous (~105 nm thick) TiO_2 films at temperatures ≤500 °C in air does not significantly degrade the photoelectrochemical performance of n-Si/TiO_2/Ni electrodes. Air-annealing much thinner (4 nm) TiO_2 films of amorphous TiO_2 on p^+-Si substrates has previously been shown to decrease the film conductivity.[12] The conduction through such thin TiO_2 films on p^+-Si in the dark is significantly affected by the annealing environment, in that films annealed in air showed a high resistance, as previously reported, whereas films annealed in forming gas exhibited much lower resistances, similar to the as-deposited films (Supporting Information Figure S10). Nyquist plots of the impedance spectra of devices with 4 nm films (Figure S10) showed that as-deposited and air-annealed samples exhibited single semicircles, indicating that no significant SiO_x interfacial layer was present and that instead the resistance was dominated by the TiO_2 layer. Thicker films (~100 nm) were observed to be conductive after air-annealing for 1 h, in contrast to the behavior of 4 nm TiO_2 films.

The rectifying properties of n-Si/TiO_2/Ni photoelectrodes are governed by the n-Si/TiO_2 junction. Evidence for this model includes the similar photovoltages generated by the same electrodes tested in 1.0 M KOH and $Fe(CN)^{3-/4-}$(aq) electrolyte, as shown in Figures 2 and 4, indicating that the rectifying junction is buried and is not influenced energetically by the redox potential of the electrolyte. Furthermore, the TiO_2/Ni junction is not rectifying because p^+-Si/TiO_2/Ni devices exhibit ohmic conduction. Thus, the Si/TiO_2 junction is the rectifying junction of interest. However, the Ni layer at the TiO_2 surface was necessary for conduction in all cases, as reported previously;[12] a separate forthcoming study shows that this effect is related to the electronic interaction at the TiO_2/Ni interface. In addition to demonstrating that crystalline TiO_2 can be an effective junction partner with n-Si, the results herein show that the V_{oc} of the n-Si/TiO_2/Ni devices was affected by the type of TiO_2 in contact with the Si and by the method of annealing. This behavior suggests that both the semiconductor/TiO_2 interface and the electronic properties of the TiO_2 can be engineered to optimize the electronic characteristics of the junction. Annealing in a reducing or oxidizing environment is a common method for controlling the electronic properties of TiO_2 via doping through changing the concentration of oxygen vacancies.[21,33] Such doping schemes alter the position of the Fermi level and can change the concentration and distribution of defects within the band gap. The observed increase in V_{oc} of forming-gas annealed samples may be due to these factors, and/or to changes in the character and density of trap states at the n-Si/SiO_x/TiO_2 interface. Further interfacial modifications or doping may allow for increased photovoltages,[34] which are required for efficient device performance.

A significant finding of this work is that the properties of TiO_2 that allow for the facile conduction of photogenerated carriers from the VB of n-Si through the TiO_2 film to the Ni catalyst are relatively general. Prior work on n-Si/TiO_2/Ni electrodes with amorphous TiO_2 suggested that midgap defect states, which were shown with XPS to exist at energy levels stretching from near the CB to the middle of the band gap, facilitate photogenerated carrier conduction through the TiO_2 film.[12] This hypothesis is in agreement with earlier studies on the dependence of current on the thickness of an amorphous TiO_2 layer in metal−insulator-semiconductor devices, which suggested that conduction arose from bulk-limited electron hopping through defect states within the TiO_2.[8] The defect states detected by Hu et al. were presumed to arise due to the amorphous structure of the TiO_2, or to nitrogen or carbon impurities remaining from the TDMAT-ALD process. The data presented herein show that various crystalline TiO_2 films, with different crystal structures, can conduct anodic current under illumination in the n-Si/TiO_2/Ni device configuration. This behavior indicates that such conduction behavior is not unique to the amorphous phase. Furthermore, SIMS data (Supporting Information Figures S11−S13) show that all the films contained carbon and nitrogen impurities, but with varying concentrations in films fabricated and processed with different methods. The sputtered films contained more carbon and nitrogen than the TDMAT-ALD films, while the TTIP-ALD films contained less carbon and nitrogen than the TDMAT-ALD films. Although impurities may contribute to increased conductivity in these materials, the impurity concentrations measured here do not linearly correlate with the conductivity of the films. For example, the sputtered films had the highest impurity content, but also exhibited the lowest through-film conductivity among the films that were fabricated and/or processed at moderate temperatures (see Supporting Information Figures S4 and S5). In addition, differences in conductivity were observed for films annealed in air or forming gas at 600 °C, despite similar carbon and nitrogen content (Supporting Information Figure S13). The impedance spectra in Supporting Information Figure S5 show that these differences are not solely due to growth of the interfacial SiO_x layer. These results suggest that carbon and nitrogen impurities are not the primary controlling factor in determining the conductivity of these various TiO_2 films within the Si/TiO_2/Ni device architecture.

Insight into the characteristics of electronically "leaky" TiO_2 can be obtained from the extensive previous literature describing the use of TiO_2 as a gate dielectric.[20,22] In these studies, Si/TiO_2/metal device structures were examined with the goal of minimizing leakage currents (which is the opposite of our goal in fabricating photoactive n-Si/TiO_2/Ni photoelectrodes for oxidative electrochemistry). TiO_2 deposited on Si by various methods was observed to have widely variable, and often large, leakage currents in the as-deposited state (usually amorphous or anatase TiO_2).[21,23,24,35] The leakage currents also depended strongly on the deposition conditions as well as on the postdeposition processing.[20] The nature of charge transport in such devices has been attributed to various factors, including high concentrations of Ti^{3+} defect states in the TiO_2[20] and thermal emission over an energy barrier within the device.[21] Furthermore, electronic transport mechanisms in Si/TiO_2/metal structures have been observed to change as a function of annealing temperature (for example, from defect-mediated Frenkel−Poole emission to a Schottky emission mechanism).[21] A common method to reduce the leakage currents is to anneal the films at temperatures between 700 and 900 °C in a pure oxygen environment, because this procedure increases the stoichiometric balance between Ti and O (thus decreasing the concentration of Ti^{3+}) and usually results in the growth of a relatively thick interfacial SiO_x layer.[21] This treatment increases the resistivity because (i) the reduction in Ti^{3+} decreases the concentration of available free carriers as well as the concentration of defect states available for defect-mediated conduction, and (ii) the increase in thickness of the SiO_x interfacial layer provides a larger tunneling resistance for charge transport. Thus, the electronic behavior of metal−

DOI: 10.1021/acsami.5b00379
ACS Appl. Mater. Interfaces 2015, 7, 15189−15199

insulator-semiconductor (MIS) devices with TiO_2 depends on the detailed fabrication and processing history of TiO_2.

We have shown herein that a variety of TiO_2 films deposited with different methods and in some cases annealed at moderate temperatures (400−500 °C) can effectively form photoactive charge-separating junctions with n-Si and can be highly conductive toward photogenerated carriers from Si. This observation is in accord with previous results on MIS devices, which have exhibited high leakage currents for various types of TiO_2. The photoemission valence spectra of the various conductive TiO_2 materials studied here (Figure 6) give further insight into the midgap defect distribution, which influences the electronic properties. The as-deposited and annealed TDMAT-ALD films of ∼100 nm thickness were all conductive within the n-Si/TiO_2/Ni electrodes, yet their midgap-defect energy distributions obtained via XPS valence measurements were clearly different. The as-deposited film exhibited a distinct peak in the photoemission signal at ∼1 eV below the Fermi level, while the forming-gas annealed TiO_2 displayed a broader photoemission from defect states having energies that spanned the band gap (with slightly elevated photoemission ∼1 eV below the Fermi level), whereas the air-annealed sample instead exhibited a tail of states close to the VB edge. Ti^{3+}-related trap states are often detected ∼0.8−2 eV below the CB edge,[8,25,26] which aligns well with the photoemission peak centered ∼1 eV below the Fermi energy in the as-deposited TiO_2. Defect states at this energy would be closely aligned with the Si VB in the heterostructure.[8] The decrease of this feature in the annealed samples is consistent with a decrease in the Ti^{3+} concentration due to annealing and crystallization of the material. The sputtered and TTIP-ALD films exhibited decreased photoemission across the band gap. These results indicate different electronic defect state concentrations and energy distributions for each of these films.

Based on previous results and the data presented herein, the observation that the different films are conductive toward photogenerated carriers from Si when they are ∼80−100 nm thick and processed at moderate temperatures suggests that they may each contain sufficient electronic defect states to allow for low-resistance charge conduction. Even though the XPS valence spectra showed different defect state distributions, all of the conductive films likely contained oxygen vacancies and associated midgap states, which may be of sufficient density to allow for conduction. Such a conclusion is in accord with a recent DFT investigation showing the possibility of hole transport through oxygen vacancy-induced defect states in amorphous TiO_2.[19] However, other conduction mechanisms, such as conventional band transport, could also be at play, and the conduction mechanisms could be different in the various TiO_2 materials.[21] Understanding the detailed conduction mechanisms in different TiO_2 materials is an important next step that would allow defects and band alignment in these electrodes to be controllably engineered for optimal performance.

Although the TiO_2 materials that were processed and annealed at moderate temperatures were shown to conduct when ∼80−100 nm thick, differences were nevertheless observed in the behavior of the various types of TiO_2. In particular, the n-Si/TiO_2/Ni samples with sputtered TiO_2 films consistently exhibited lower open-circuit voltages than the other samples, and such films showed an increase in resistance as the TiO_2 thickness was varied from ∼25 nm to ∼180 nm (as manifested by a decrease in fill factor in the $J-E$ data; see Supporting Information Figure S4). This behavior is in contrast to that of n-Si/TiO_2/Ni electrodes with as-deposited TDMAT-ALD TiO_2, which have previously been shown to exhibit thickness-independent $J-E$ slopes for TiO_2 thicknesses between ∼4 and ∼150 nm,[12] indicating that the conductivity of these films is high enough that the resistance of even the thickest TiO_2 layers does not limit the conduction. Four-point probe measurements showed that sputtered films had conductivities about 2 orders of magnitude higher than the as-deposited TDMAT-ALD films. However, if conduction through the TiO_2 in n-Si/TiO_2/Ni electrodes occurs via defect bands in the TiO_2 in both cases, this behavior can be understood if there is a larger effective resistivity for defect band conduction in the sputtered films. Such a phenomenon would not necessarily be interrogated with four-point probe measurements.

The diminished performance of TDMAT-ALD samples that were annealed in air or forming gas at higher temperatures (600 or 775 °C) is likely due to a decrease in the conductivity of the TiO_2 layer as well as to the increased resistance due to the growth of SiO_x interfacial layers. The impedance spectra of these samples (Supporting Information Figure S5) support this conclusion, as the presence of two semicircles in the Nyquist plots for the 600 °C-annealed samples suggests the growth of an additional interfacial layer with different impedance response. Furthermore, the diameters of both semicircles from the 600 °C-air-annealed sample are larger than the 600 °C-forming-gas annealed sample, indicating that air annealing increases the resistance of the TiO_2 as well as the interfacial layer. TEM imaging showed that the interfacial SiO_x layers in the samples annealed at 600 °C are slightly thicker (t = 1.7−2.0 nm) than those in the conductive samples annealed at 450 °C, but the interfacial layers in the latter samples have lower tunneling resistance (as indicated by the lack of separate semicircles in the impedance spectra, Figure S5a). The interfacial films in samples annealed at 775 °C were thicker (up to t = 6.0 nm in air-annealed samples), which significantly increased the resistance in these electrodes. In addition, the majority rutile phase (rather than anatase) in these samples may also influence the conduction.

The stability data presented in Figure 7 showed that films with different crystallinity and grain size protected the underlying Si from anodic photocorrosion, with the exception of the TTIP-ALD films, which had a nonuniform thickness as well as physical imperfections (cracks). Amorphous TiO_2 films deposited using ALD are seemingly an ideal protective coating, because the ALD process produces conformal films and the amorphous structure does not contain extended defects such as grain boundaries that could act as initiation points for corrosion-related damage. However, the >60 h photocurrent stability of samples with sputtered and annealed films indicates that an amorphous structure is not unique for either stabilization or the formation of the heterojunction at the n-Si/TiO_2 interface. Furthermore, the observations reported herein indicate that TiO_2 films with through-thickness grain boundaries can still serve as viable protection layers. Si is known to undergo photoanodic passivation in alkaline conditions, which could allow for stability even in the presence of pinholes in these films, because the Si does not dissolve. In contrast, the larger cracks and fissures between grains (for example, as seen in Figure 5c) in the TTIP-ALD films are detrimental to long-term stability of the Si photoelectrode. Large portions of the TTIP-ALD films were missing from the Si

DOI: 10.1021/acsami.5b00379
ACS Appl. Mater. Interfaces 2015, 7, 15189−15199

after the stability tests, indicating possible underetching, delamination, and mechanical damage. Such observations reflect the necessity of using compact films for photocorrosion protection.

CONCLUSIONS

Various fabrication methods were used to deposit TiO_2 films on n-Si to form n-Si/TiO_2/Ni photoanodes for water oxidation. Characterization of the TiO_2 films showed that they exhibited different crystallinity, structure, and defect state energy distributions. When used as photoanodes in an alkaline electrolyte or in aqueous $Fe(CN)_6^{3-/4-}$, these electrodes exhibited rectifying $J-E$ characteristics regardless of the type of TiO_2 used when grown or processed at moderate temperatures. In addition, the V_{oc} under illumination of electrodes with ALD-deposited TiO_2 depended on the postdeposition annealing environment (forming gas versus air), indicating that the junction properties can be tuned. All of the compact films that were ~100 nm thick protected Si against photocorrosion during water oxidation, but films with physical defects, such as cracks, produced significant degradation in the properties of the photoanode over 60 h of operation. These results show the generality of using TiO_2 as a rectifying contact to n-Si, and suggest that the Si/TiO_2 interface can be engineered to improve junction properties and/or the TiO_2 can be modified for improved performance.

ASSOCIATED CONTENT

Supporting Information

Detailed methods, XRD data, Raman data, XPS data, TEM data, SIMS data, and photoelectrochemical data. The Supporting Information is available free of charge on the ACS Publications website at DOI: 10.1021/acsami.5b00379.

AUTHOR INFORMATION

Corresponding Author

*E-mail: nslewis@caltech.edu.

Notes

The authors declare no competing financial interest.

ACKNOWLEDGMENTS

This material is based upon work performed at the Joint Center for Artificial Photosynthesis, a DOE Energy Innovation Hub, supported through the Office of Science of the U.S. Department of Energy under Award No. DE-SC0004993. XPS data were collected at the Molecular Materials Research Center of the Beckman Institute of the California Institute of Technology. TEM data were collected at the Caltech Transmission Electron Microscopy Facility. A.I.C. recognizes a Graduate Research Fellowship from the National Science Foundation for support. The authors gratefully acknowledge the assistance of Dr. Yunbin Guan during collection of SIMS data.

REFERENCES

(1) Lewis, N. S.; Nocera, D. G. Powering the Planet: Chemical Challenges in Solar Energy Utilization. *Proc. Natl. Acad. Sci. U. S. A.* **2006**, *103*, 15729–15735.

(2) Walter, M. G.; Warren, E. L.; McKone, J. R.; Boettcher, S. W.; Mi, Q.; Santori, E. A.; Lewis, N. S. Solar Water Splitting Cells. *Chem. Rev.* **2010**, *110*, 6446–6473.

(3) Haussener, S.; Xiang, C.; Spurgeon, J. M.; Ardo, S.; Lewis, N. S.; Weber, A. Z. Modeling, Simulation, and Design Criteria for Photoelectrochemical Water-Splitting Systems. *Energy Environ. Sci.* **2012**, *5*, 9922–9935.

(4) Khaselev, O.; Turner, J. A. A Monolithic Photovoltaic-Photoelectrochemical Device for Hydrogen Production Via Water Splitting. *Science* **1998**, *280*, 425–427.

(5) Fujishima, A.; Honda, K. Electrochemical Photolysis of Water at a Semiconductor Electrode. *Nature* **1972**, *238*, 37–38.

(6) Tilley, S. D.; Cornuz, M.; Sivula, K.; Gratzel, M. Light-Induced Water Splitting with Hematite: Improved Nanostructure and Iridium Oxide Catalysis. *Angew. Chem., Int. Ed.* **2010**, *49*, 6405–6408.

(7) Chen, Y. W.; Prange, J. D.; Duhnen, S.; Park, Y.; Gunji, M.; Chidsey, C. E. D.; McIntyre, P. C. Atomic Layer-Deposited Tunnel Oxide Stabilizes Silicon Photoanodes for Water Oxidation. *Nat. Mater.* **2011**, *10*, 539–544.

(8) Scheuermann, A. G.; Prange, J. D.; Gunji, M.; Chidsey, C. E. D.; McIntyre, P. C. Effects of Catalyst Material and Atomic Layer Deposited TiO_2 Oxide Thickness on the Water Oxidation Performance of Metal–Insulator–Silicon Anodes. *Energy Environ. Sci.* **2013**, *6*, 2487–2496.

(9) Strandwitz, N. C.; Comstock, D. J.; Grimm, R. L.; Nichols-Nielander, A. C.; Elam, J.; Lewis, N. S. Photoelectrochemical Behavior of n-Type Si(100) Electrodes Coated with Thin Films of Manganese Oxide Grown by Atomic Layer Deposition. *J. Phys. Chem. C* **2013**, *117*, 4931–4936.

(10) Kenney, M. J.; Gong, M.; Li, Y.; Wu, J. Z.; Feng, J.; Lanza, M.; Dai, H. High-Performance Silicon Photoanodes Passivated with Ultrathin Nickel Films for Water Oxidation. *Science* **2013**, *342*, 836–840.

(11) Mei, B.; Seger, B.; Pedersen, T.; Malizia, M.; Hansen, O.; Chorkendorff, I.; Vesborg, P. C. K. Protection of p^+-n-Si Photoanodes by Sputter-Deposited Ir/IrO_x thin Films. *J. Phys. Chem. Lett.* **2014**, *5*, 1948–1952.

(12) Hu, S.; Shaner, M. R.; Beardslee, J. A.; Lichterman, M. F.; Brunschwig, B. S.; Lewis, N. S. Amorphous TiO_2 Coatings Stabilize Si, GaAs and GaP Photoanodes for Efficient Water Oxidation. *Science* **2014**, *344*, 1005–1009.

(13) Lichterman, M. F.; Carim, A. I.; McDowell, M. T.; Hu, S.; Gray, H. B.; Brunschwig, B. S.; Lewis, N. S. Stabilization of n-Cadmium Telluride Photoanodes for Water Oxidation to O_2(g) in Aqueous Alkaline Electrolytes Using Amorphous TiO_2 films Formed by Atomic-Layer Deposition. *Energy Environ. Sci.* **2014**, *7*, 3334–3337.

(14) McDowell, M. T.; Lichterman, M. F.; Spurgeon, J. M.; Hu, S.; Sharp, I. D.; Brunschwig, B. S.; Lewis, N. S. Improved Stability of Polycrystalline Bismuth Vanadate Photoanodes by Use of Dual-Layer Thin TiO_2/Ni Coatings. *J. Phys. Chem. C* **2014**, *118*, 19618–19624.

(15) Yang, J.; Walczak, K.; Anzenberg, E.; Toma, F. M.; Yuan, G.; Beeman, J.; Schwartzberg, A.; Lin, Y.; Hettick, M.; Javey, A.; Ager, J. W.; Yano, J.; Frei, H.; Sharp, I. D. Efficient and Sustained Photoelectrochemical Water Oxidation by Cobalt Oxide/Silicon Photoanodes with Nanotextured Interfaces. *J. Am. Chem. Soc.* **2014**, *136*, 6191–6194.

(16) Sun, K.; McDowell, M. T.; Nielander, A. C.; Hu, S.; Shaner, M. R.; Yang, F.; Brunschwig, B. S.; Lewis, N. S. Stable Solar-Driven Water Oxidation to O_2(g) by Ni-Oxide-Coated Silicon Photoanodes. *J. Phys. Chem. Lett.* **2015**, *6*, 592–598.

(17) Sun, K.; Saadi, F. H.; Lichterman, M. F.; Hale, W. G.; Wang, H.-P.; Zhou, X.; Plymale, N. T.; Omelchenko, S. T.; He, J.-H.; Papadantonakis, K. M.; Brunschwig, B. S.; Lewis, N. S. Stable Solar-Driven Oxidation of Water by Semiconducting Photoanodes Protected by Transparent Catalytic Nickel Oxide Films. *Proc. Natl. Acad. Sci. U. S. A.* **2015**, *112*, 3612–3617.

(18) Lichterman, M. F.; Shaner, M. R.; Handler, S. G.; Brunschwig, B. S.; Gray, H. B.; Lewis, N. S.; Spurgeon, J. M. Enhanced Stability and Activity for Water Oxidation in Alkaline Media with Bismuth Vanadate Photoelectrodes Modified with a Cobalt Oxide Catalytic Layer Produced by Atomic Layer Deposition. *J. Phys. Chem. Lett.* **2013**, *4*, 4188–4191.

DOI: 10.1021/acsami.5b00379
ACS Appl. Mater. Interfaces 2015, 7, 15189–15199

(19) Pham, H. H.; Wang, L. W. Oxygen Vacancy and Hole Conduction in Amorphous TiO_2. *Phys. Chem. Chem. Phys.* **2014**, *17*, 541−550.
(20) Wilk, G. D.; Wallace, R. M.; Anthony, J. M. High-K Gate Dielectrics: Current Status and Materials Properties Considerations. *J. Appl. Phys.* **2001**, *89*, 5243−5275.
(21) Yang, W.; Marino, J.; Monson, A.; Wolden, C. A. An Investigation of Annealing on the Dielectric Performance of TiO_2 Thin Films. *Semicond. Sci. Technol.* **2006**, *21*, 1573−1579.
(22) Campbell, S. A.; Kim, H.-S.; Gilmer, D. C.; He, B.; Ma, T.; Gladfelter, W. L. Titanium Dioxide (TiO_2)-Based Gate Insulators. *IBM J. Res. Dev.* **1999**, *43*, 383−392.
(23) Lee, B. H.; Jeon, Y.; Zawadzki, K.; Qi, W.-J.; Lee, J. Effects of Interfacial Layer Growth on the Electrical Characteristics of Thin Titanium Oxide Films on Silicon. *Appl. Phys. Lett.* **1999**, *74*, 3143−3145.
(24) Rausch, N.; Burte, E. P. Thin High-Dielectric TiO_2 Films Prepared by Low Pressure MOCVD. *Microelectron. Eng.* **1992**, *19*, 725−728.
(25) Kurtz, R. L.; Stockbauer, R.; Madey, T. E.; Roman, E.; de Segovia, J. L. Synchrotron Radiation Studies of H_2O Adsorption on TiO_2(110). *Surf. Sci.* **1989**, *218*, 178−200.
(26) Henderson, M. A.; Epling, W. S.; Peden, C. H. F.; Perkins, C. L. Insights into Photoexcited Electron Scavenging Processes on TiO_2 Obtained from Studies of the Reaction of O_2 with OH Groups Adsorbed at Electronic Defects on TiO_2(110). *J. Phys. Chem. B* **2003**, *107*, 534−545.
(27) Zhang, W. F.; He, Y. L.; Zhang, M. S.; Yin, Z.; Chen, Q. Raman Scattering Study on Anatase TiO_2 Nanocrystals. *J. Phys. D: Appl. Phys.* **2000**, *33*, 912−916.
(28) Lin, F.; Boettcher, S. W. Adaptive Semiconductor/Electrocatalyst Junctions in Water-Splitting Photoanodes. *Nat. Mater.* **2014**, *13*, 81−86.
(29) Trotochaud, L.; Young, S. L.; Ranney, J. K.; Boettcher, S. W. Nickel-Iron Oxyhydroxide Oxygen-Evolution Electrocatalysts: The Role of Intentional and Incidental Iron Incorporation. *J. Am. Chem. Soc.* **2014**, *136*, 6744−6753.
(30) Weinberger, B. R.; Garber, R. B. Titanium Dioxide Photocatalysts Produced by Reactive Magnetron Sputtering. *Appl. Phys. Lett.* **1995**, *66*, 2409−2411.
(31) Johnson, A. M.; Stair, P. C. Alternative Low-Pressure Surface Chemistry of Titanium Tetraisopropoxide on Oxidized Molybdenum. *J. Phys. Chem. C* **2014**, *118*, 29361−29369.
(32) Shaner, M. R.; Hu, S.; Sun, K.; Lewis, N. S. Stabilization of Si Microwire Arrays for Solar-Driven H_2O Oxidation to O_2(g) in 1.0 M KOH(aq) Using Conformal Coatings of Amorphous TiO_2. *Energy Environ. Sci.* **2015**, *8*, 203−207.
(33) Sekiya, T.; Yagisawa, T.; Kamiya, N.; Das Mulmi, D.; Kurita, S.; Murakami, Y.; Kodaira, T. Defects in Anatase TiO_2 Single Crystal Controlled by Heat Treatments. *J. Phys. Soc. Jpn.* **2004**, *73*, 703−710.
(34) Perego, M.; Seguini, G.; Scarel, G.; Fanciulli, M.; Wallrapp, F. Energy Band Alignment at TiO_2/Si Interface with Various Interlayers. *J. Appl. Phys.* **2008**, *103*, 043509−043509−6.
(35) Yan, J. Structural and Electrical Characterization of TiO_2 Grown from Titanium Tetrakis-Isopropoxide (TTIP) and TTIP/H_2O Ambients. *J. Vac. Sci. Technol., B: Microelectron. Nanometer Struct.–Process., Meas., Phenom.* **1996**, *14*, 1706−1711.

NOTE ADDED AFTER ASAP PUBLICATION

This paper was published on the Web on July 7, 2015. Additional text corrections and the replacement of the Abstract graphic and Figure 2 were implemented, and the paper was reposted on July 8, 2015.

DOI: 10.1021/acsami.5b00379
ACS Appl. Mater. Interfaces 2015, 7, 15189−15199